Computational and Structural Biotechnology Journal 21 (2023) 1157–1168

Contents lists available at ScienceDirect

Computational and Structural Biotechnology Journal

journal homepage: www.elsevier.com/locate/csbj

Spatial patterns of the cap-binding complex eIF4F in human melanoma cells

Xinpu Tang [a,b,c,1], Yi Pu [a,d,1], Haoning Peng [a,e], Kaixiu Li [a], Sara Faouzi [f], Tianjian Lu [a,e], Dan Pu [g], Michael Cerezo [h,i], Jianguo Xu [b], Lu Li [g,*], Caroline Robert [f,j,**], Shensi Shen [a,c,e,***]

[a] Institute of Thoracic Oncology, West China Hospital of Sichuan University, Chengdu, China
[b] Department of Neurosurgery, West China Hospital of Sichuan University, Chengdu, China
[c] National Clinical Research Center for Geriatrics, West China Hospital, Sichuan University, Chengdu, China
[d] Department of Burn Surgery, West China Hospital of Sichuan University, Chengdu, China
[e] Department of Thoracic Surgery, West China Hospital of Sichuan University, Chengdu, China
[f] INSERM U981, Gustave Roussy Cancer Campus, Villejuif, France
[g] Lung Cancer Center, West China Hospital of Sichuan University, Chengdu, China
[h] Université Côte d'Azur, Nice, France
[i] Centre Méditerranéen de Médicine Moléculaire (C3M), INSERM U1065, Equipe 12, Nice, France
[j] Dermatology Unit, Gustave Roussy Cancer Campus, Villejuif, France

ARTICLE INFO

Article history:
Received 3 September 2022
Received in revised form 27 January 2023
Accepted 29 January 2023
Available online 31 January 2023

ABSTRACT

As a central node of protein synthesis, the cap-binding complex, eukaryotic translation initiation factor 4 F (eIF4F), is involved in cell homeostasis, development and tumorigenesis. A large body of literature exists on the regulation and function of eIF4F in cancer cells, however the intracellular localization patterns of this complex are largely unknown. Since different subsets of mRNAs are translated in distinct subcellular compartments, understanding the distribution of translation initiation factors in the cell is of major interest. Here, we developed an *in situ* detection method for eIF4F at the single cell level. By using an image-based spot feature analysis pipeline as well as supervised machine learning, we identify five distinct spatial patterns of the eIF4F translation initiation complex in human melanoma cells. The quantity of eIF4F complex per cell correlated with the global mRNA translation activity, and its variation is dynamically regulated by cell state or extracellular stimuli. In contrast, the spatial patterns of eIF4F complexes at the single cell level could distinguish melanoma cells harboring different oncogenic driver mutations. This suggests that different tumorigenic contexts differentially regulate the subcellular localization of mRNA translation, with specific localization of eIF4F potentially associated with melanoma cell chemoresistance.

1. Introduction

Post-transcriptional fine-tuning of gene expression in response to signaling cues requires precise spatio-temporal control of mRNA translation. This was first characterized by Lawrence and Singer, who observed localized translation of *actin* mRNA in chicken fibroblasts using *in situ* hybridization [25], and was subsequently shown in other organisms such as mammalian neurons and oligodendrocytes [21,23]. In mammalian cells, localized mRNA translation is thought to be crucial for cellular homeostasis, differentiation and development. Indeed, localized mRNA translation is involved in proper cell polarization and motility, mainly through localized translation of mRNA encoding actin and related cytoskeleton proteins at the leading cellular edge. It is also implicated in axonal growth and synaptic plasticity of neurons [42]. In addition, local mRNA translation is involved in the targeting of nascent peptides to the endoplasmic reticulum [1,32]. Recent high-resolution imaging technologies that detect mRNAs and their translation states have demonstrated the existence of translation hotspots in specific subcellular compartments [10]. Pioneering work by Battich et al., showed high

* Corresponding author.
** Corresponding author at: INSERM U981, Gustave Roussy Cancer Campus, Villejuif, France.
*** Correspondence to: Institute of Thoracic Oncology and National Clinical Research Center for Geriatrics, West China Hospital, Sichuan University, Chengdu, China.
E-mail addresses: windflower1991@vip.163.com (L. Li), Caroline.Robert@gustaveroussy.fr (C. Robert), shenshensi@wchscu.cn (S. Shen).
[1] These authors contributed equally to this work.

https://doi.org/10.1016/j.csbj.2023.01.040

heterogeneity of mRNA localization in human cells by using high-throughput single-molecule fluorescence *in situ* hybridization (smFISH) [3]. More recently, using a dual protein-mRNA localization screen, Chouaib et al., showed that 32 mRNAs displayed specific cytoplasmic localizations. They unexpectedly found that mRNA localization frequently requires ongoing translation, suggesting widespread co-translational RNA targeting mechanisms [9]. These results suggest that mRNA localization, by facilitating nascent protein localization, is a critical optimization element of cellular functions and metabolism. In contrast to the increasing knowledge concerning mRNA localization, little is known regarding the subcellular localization of the translation initiation factors.

The decoding of genetic messages from mRNAs to polypeptides occurs in three steps: initiation, elongation and termination. The initiation step, intricately controlled by several initiation factors, is the rate-limiting step of mRNA translation [8]. At the beginning of translation initiation, the eukaryotic initiation factor 4 F (eIF4F) complex, comprising eIF4E, eIF4G and eIF4A, binds directly to the cap structure at the mRNA terminus of the 5′ untranslated region (5′UTR) *via* cap-binding protein eIF4E [28]. In activated platelets, eIF4F is re-distributed to the mRNA-rich areas in the cytoskeletal core, an event mitigated by disruption of the actin cytoskeleton [26]. In addition, in neuronal dendrites, eIF4E in mRNA-containing granules associates with two distinct actin networks, specifically long filaments and dendritic spine heads with branched short filaments [39]. Apart from the cap-recognizing factor eIF4E, eIF4G can also localize to RNA granules on oligodendrocytes [2] and stress granules [22]. Moreover, eIF4G also co-localizes with paxillin in the endoplasmic reticulum at the leading edge of migrating fibroblasts [46]. These earlier works thus raise intriguing questions concerning the intracellular topology of localized mRNA translation machineries. In particular, the potential impact of eIF4F localization in cancer cells has not been studied so far.

We recently developed a single-cell level *in situ* detection method for the eIF4F complex by using a proximity ligation assay [37]. Here, we further systemically analyzed the localization of eIF4F and the heterogeneity of spatial patterning of the initiation complex both in BRAF mutated and NRAS mutated melanoma cells. By adapting an image-based single molecule analysis pipeline and machine learning, we defined five cellular phenoclusters of the actively translating eIF4F complex that could potentially distinguish melanoma cells harboring different driver mutations. In addition, we further explored the heterogeneity of eIF4F phenoclusters in multiple human melanoma cell lines and found that specific eIF4F localization patterns may be related to chemoresistance in cancer treatment.

2. Results

2.1. The quantity of the eIF4E-eIF4G complex correlates with protein synthesis activity in situ

To probe the formation of the eIF4F complex and its subcellular localization, we developed a proximity ligation assay (PLA)-based procedure allowing the direct *in situ* visualization of the eIF4E-eIF4G protein complex as a surrogate of the eIF4F cap binding complex [5] (Fig. 1**A**). By using antibodies recognizing the cap-binding factor eIF4E and the scaffold protein eIF4G, *in situ* polymerase chain reactions at the single-molecule level can be performed specifically when eIF4E and eIF4G interact (distance < 40 nm) (Fig. 1**A**, left panel) [37]. We adapted a Matlab-based iterative cell segmentation pipeline [29] to precisely quantify the intracellular eIF4E-eIF4G complex (Fig. 1**A**, right panel and **Supplementary Fig. S1A**). We validated the antibody specificity by knocking down eIF4E or eIF4G1, and showed a dramatic decrease of the eIF4E-eIF4G PLA complex in both conditions (**Supplementary Fig. S1B-C**). To test whether the quantity of eIF4E-eIF4G reflects the cellular mRNA translation activity, we performed polysome profiling following two classical treatments that are known to regulate mRNA translation: mTOR inhibition and nutrient starvation. As shown in Fig. 1**B-C**, both inhibition of mTOR by PP242 [20] and nutrient starvation by cell culture in HBSS [38] inhibited global mRNA translation with an accumulation of the monosomal 80 S fraction and a decrease in the polysomal fractions (**Supplementary Fig. S2A**). Accordingly, we found that the quantity of the eIF4E-eIF4G complex significantly decreased upon mTOR inhibition or nutrient starvation (Fig. 1**B-C**, right panel). This reveals that *in situ* PLA-based detection of eIF4E-eIF4G in its activated status is directly correlated with cellular translational activity. We have recently shown that BRAF inhibition dramatically decreases the number of active eIF4F complexes in $BRAF^{V600E}$ melanoma cells sensitive to BRAF inhibitors [5]. To further test our PLA-based image analysis pipeline, we treated A375 melanoma cells with BRAF inhibitor (1 μM vemurafenib) and confirmed that the number of eIF4E-eIF4G complexes was dramatically decreased upon BRAF inhibition (Fig. 1**D-E**). Consistent with a complete inhibition of the BRAF-MAPK-ERK pathway downstream of BRAF, we observed nuclear translocation of ERK kinase translocation reporters (ERK-KTR)(**Supplementary Fig. S2B**) [35] in the individual BRAF mutant cells treated with BRAF inhibitor (Fig. 1**D-C** and **Supplementary Fig. S2C-E**). In addition to the observations showed above, the concentration of eIF4A is almost 10 times that of either eIF4E or eIF4G and that the primary regulation of eIF4F is *via* 4E-BP and therefore, it is highly likely that the eIF4E-eIF4G complex is truly representative of eIF4F.

2.2. PLA-based spatial pattern analysis pipeline for the eIF4E-eIF4G complex

To obtain a high-content single cell analysis of eIF4E-eIF4G spatial patterns, we acquired images in three *z* planes, with a step size of 1 μm, covering the full cellular height at a minimum of three sites on each slide, followed by maximum-intensity projection of z stacks for eIF4E-eIF4G spot detection. By adapting a mRNA smFISH spot analysis tool [3], the acquired images were then subjected to Matlab-based cell segmentation and eIF4E-eIF4G PLA spot detection (Fig. 1**F, Supplementary Fig. S3 and Supplementary Fig. S4A**). As an illustration of the pipeline, Fig. 1G shows the distance of each spot to the cell membrane in each cell (Fig. 1**G and Supplementary Fig. S4B**). Altogether, we extracted ~13 macro features of eIF4E-eIF4G spots in the corresponding cell. These comprise: 1) the number of eIF4E-eIF4G spots in each cell, 2) each spot localization with respect to the cell membrane or centroid, 3) each spot localization with respect to the nuclear center projected from the cell outline, 4) the mean value and variation of spot-to-spot distance in a single cell, 5) the number of spots within a given radius ranging from 5% to 75% of given points within the cell, 6) the number of spots within a range of image pixels (20–120 pixels) from a given spot in the same cell, 7) cell or nuclear area shape and main axis, and 8) cell Zernik features (Fig. 1**H**). This analysis of large-scale image features using a large number of single cells allowed us to explore the eIF4E-eIF4G spatial patterns in human melanoma cells.

2.3. The quantity of eIF4E-eIF4G complexes cannot distinguish BRAF and NRAS mutated melanoma cells

We then performed the eIF4E-eIF4G proximity ligation assay in twelve human melanoma cell lines comprising melanoma cells harboring the $BRAF^{V600E}$ mutation or $NRAS^{Q61R}$ mutation, and one BRAF/NRAS wild-type melanoma cell line, MeWo (Fig. 2**A**). Among the BRAF mutated melanoma cell lines, A2058 ($BRAF^{V600E}$/$TP53^{V274F}$/$TP63^{R379C}$), Mel624($BRAF^{V600E}$/$TP53^{C275W}$) and Malme3M-R ($BRAF^{V600E}$), which are resistant to anti-BRAF targeted therapy, showed a trend towards a higher quantity of eIF4E-eIF4G complexes,

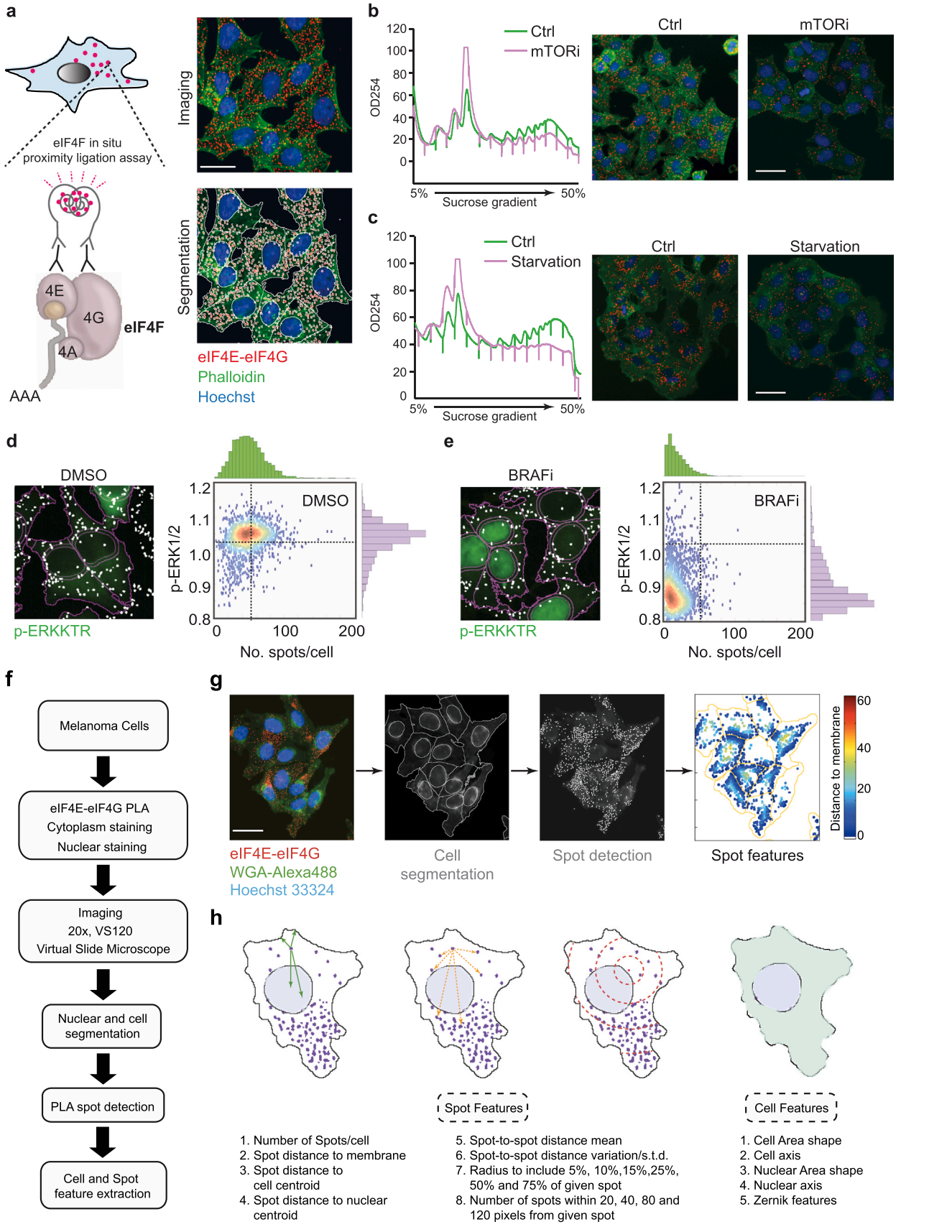

(caption on next page)

Fig. 1. *In situ* detection of eIF4F subcellular distribution. (A) Left panel: schematic view of the proximity ligation assay for the eIF4E-eIF4G complex. 4E: eIF4E, 4 G: eIF4G, 4 A: eIF4A, AAA: polyA tail. Right panel: example images of the eIF4E-eIF4G PLA assay and cell segmentation. The eIF4E-eIF4G complex was stained following the proximity ligation assay protocol, the cytoskeleton was stained by Phalloidin-Alexa 488, and the nucleus was stained with Hoechst 33342. (B) Polysome profile and eIF4E-eIF4G PLA assay of A375 cells upon treatment with PP242. Cells were treated with PP424 at 1 μM for 24 h, and then lysed by polysome hypotonic buffer or fixed with 4% PFA. (C) Polysome profile and eIF4E-eIF4G PLA assay of QBC989 cholangiocarcinoma cells upon nutrient deprivation. Cells were cultured with HBSS solution for nutrient starvation for 16 h, followed by hypotonic buffer lysis or 4% PFA fixation. (D-E) A375 cells expressing the ERK-KTR reporter gene were treated with 1 μM vemurafenib for 24 h and the eIF4E-eIF4G PLA assay was performed. Single cell quantification of ERK-KTR nuclear translocation (p-ERK1/2) and eIF4E-eIF4G spot count are plotted. (F) Pipeline of the eIF4E-eIF4G PLA image analysis. The eIF4E-eIF4G complex was stained following the proximity ligation assay protocol, the cytoskeleton was stained with Phalloidin-Alexa 488, and the nucleus was stained with Hoechst 33342. Cell images were then subjected to Cellprofiler 2.0 analysis to identify the nucleus and cytoplasm. The eIF4E-eIF4G spots were identified by using Cellprofiler module 'IdentifySpots.m' followed by correlation with each cell. The localization pattern of the eIF4E-eIF4G spots was calculated with Cellprofiler module 'MeasureLocalizationOfSpots.m'. (G) Example images of the cell segmentation and spot localization analysis. (H) Summary of the spot features and cell features measured by Cellprofiler 2.0.

although it was not statistically significant compared to those in BRAF mutated melanoma cells such as A375 ($BRAF^{V600E}$/$CDKN2A^{E61Ter}$), Malme3M-S and SKMEL-28($BRAF^{V600E}$/$CDK4^{R24C}$/$EGFR^{P753S}$/$PTEN^{T167A}$). The BRAF/NRAS wild-type melanoma cell line showed a higher number and variation of eIF4E-eIF4G protein complexes (Fig. 2**B and Supplementary Fig. S5**). The association between eIF4E-eIF4G quantity and sensitivity to BRAF inhibition is consistent with our previous report implicating eIF4F in the chemoresistance of BRAF mutated melanoma [5]. Although NRAS mutated melanoma cells tended to have a higher variability of the number of eIF4E-eIF4G complexes, with the highest variation observed in M311 melanoma cells (**Supplementary Fig. S5G)**, neither the quantity nor the variation of the number of eIF4E-eIF4G complexes could distinguish between melanoma cells harboring different driver mutations.

However, we observed heterogeneous spatial patterns at the single-cell level even within the same cell line. We thus performed a non-supervised hierarchical clustering of the eIF4E-eIF4G spot features upon image analysis (Fig. 2**C and Supplementary Fig. S6A**). This allowed us to cluster different individual cells based on their eIF4E-eIF4G subcellular distribution, for instance, based on feature 13 (mean distance to the nuclear center) and feature 39 (distribution of spots within a range of radius of a given spot). Using this approach, typical cells could be clustered into two phenotypes: eIF4E-eIF4G spots are localized close to the cell outline in a polarized fashion (cell_1, 2, 3 in Fig. 2**D**), whereas in typical cell_4, cell_5 and cell_6, eIF4E-eIF4G spots are localized closely around the nuclear membrane (Fig. 2**D and Supplementary Fig. S6B**). These typical cells are not from the same cell line, suggesting that the spatial cellular patterns of eIF4E-eIF4G complexes could be shared among different melanoma cell lines.

2.4. Support-vector machine-based machine learning defines five cellular spatial patterns of eIF4E-eIF4G complexes

We applied a support-vector machine (SVM)-based machine learning algorithm with the aim of defining a landscape of the subcellular spatial patterns of the eIF4E-eIF4G complex in human melanoma cells (Fig. 3**A**). To be sure that sampled cells could represent the full range of the ~13 macro features of the eIF4E-eIF4G complex and could account for potential overrepresentation of certain eIF4E-eIF4G spatial patterns due to more abundant cell shapes or sizes, we devised a two-step sampling process. By gathering all the ~1.2×10^4 melanoma cells from the eleven cell lines, we first randomly sampled 30% of the total number of cells from the initial pool of single cells and then computed the pairwise Euclidean distance of features in the ~13 macro feature space after z-score normalization. Following this sampling, we calculated the number of neighbors of each cell by defining a distance of neighboring to ensure each cell had at least one neighbor. This two-step sampling generated ~5000 cells per cell clustering run. As shown in Fig. 3**B**, we found five clusters of eIF4E-eIF4G spatial patterns in melanoma cells with the area under curve (AUC) of the receiver operating characteristic curve (ROC) over 0.8 in each cluster (**Supplementary Fig. S7**). In total, cluster 1 represented the most frequent phenotype in all the melanoma cells (29.8%), followed by cluster 3 accounting for 26.5% of all the melanoma cells. The cluster 5 phenotype of the eIF4E-eIF4G complex was the least represented, accounting for only 9.7% of all the melanoma cells (Fig. 3**C**).

To define the main eIF4E-eIF4G spatial patterns, we then calculated the centroid for each obtained cluster and grouped each cells using supervised clustering (Fig. 3**D**). This defined five spot localization types that we termed eIF4E-eIF4G complex phenoclusters. These five phenoclusters of the eIF4E-eIF4G complex were comprised of: 1) a distal dispersed spot pattern featuring relatively longer distances from spots to the cell centroids or nuclear centroids and a larger radius including numerous spots (Figs. 3**D**, 1: Distal dispersed), this pattern represented eIF4E-eIF4G complexes distributed close to the cell membrane. 2) Proximal grouped spot localization with relatively longer distances to cell outline and shortest distances to the cell and nuclear centroids, accompanied by a higher fraction of spots within a radius of over 40 pixels. In this phenocluster, the eIF4E-eIF4G protein complexes formed grouped clusters close to the nucleus (Figs. 3**D**, 2: Proximal grouped). 3) Proximal dispersed spot localization, compared to phenocluster 2. This localization type showed median distances to the cell outline with a much lower fraction of spots within a radius less than 40 pixels. Therefore, the cells showed a distribution of eIF4E-eIF4G complexes in a dispersed manner closer to the nuclear membrane (Figs. 3**D**, 3: Proximal dispersed). 4) Spread out spot pattern with general low scores of all the measured features, particularly the distance between each spot was equally low, indicating that the eIF4E-eIF4G complexes were distributed equally in the cytoplasm (Figs. 3**D**, 4: Spread out). 5) Distal polarized spot localization, which showed an extremely high number of spots with a fixed radius and long distances to the cell and nuclear centroids, with a distribution of eIF4E-eIF4G complexes polarized to one part of the cell and far from the cell center (Figs. 3**D**, 5: Distal polarized).

2.5. Features of eIF4E-eIF4G spatial patterns can distinguish between melanoma cells harboring different driver mutations

Since the quantity of eIF4E-eIF4G protein complexes could not distinguish between the mutation patterns of melanoma cells, we wondered whether the localization patterns of the eIF4E-eIF4G complexes correlated with various driver mutations. Due to the high variability of the eIF4E-eIF4G localization patterns in each melanoma cell line, we first performed a principal component analysis based on the SVM model features that defined the five main phenoclusters in Fig. 3**D**. This process allowed us to select the first ten principal components that accounted for most of the image feature variations (> 93%) (Fig. 3**E**). Following this dimension reduction of the melanoma cell eIF4E-eIF4G complex localization features, we applied hierarchical clustering based on the average Euclidean distance of the ten principal components of each cell line. We showed that the eIF4E-eIF4G spot spatial patterns of the eleven melanoma cell lines could be classified into two major clusters (Fig. 3**F**). One cluster comprised all the $BRAF^{V600E}$ mutated melanoma cell lines

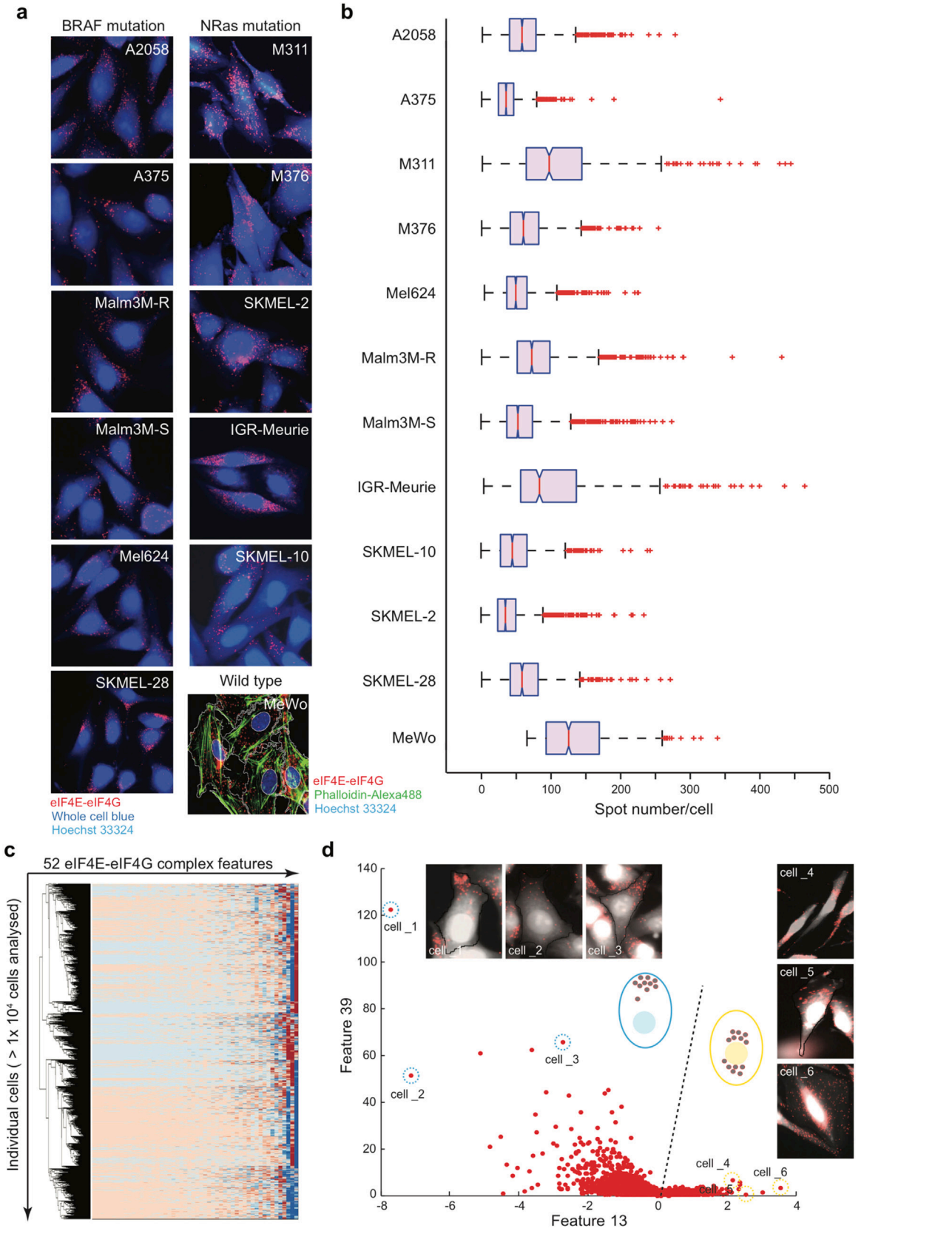

Fig. 2. Detection of eIF4E-eIF4G complexes in eleven melanoma cell lines. (A) Example images of eIF4E-eIF4G complex PLA staining in different melanoma cell lines. (B) Quantification of the eIF4E-eIF4G spot count in melanoma cell lines. (C) Hierarchical clustering of all the eIF4E-eIF4G spot features of single melanoma cells. (D) Simple plot of spot feature 13 and spot feature 39 to distinguish the localization of eIF4E-eIF4G complexes. The subset images correspond to the cells marked out on the dot plot.

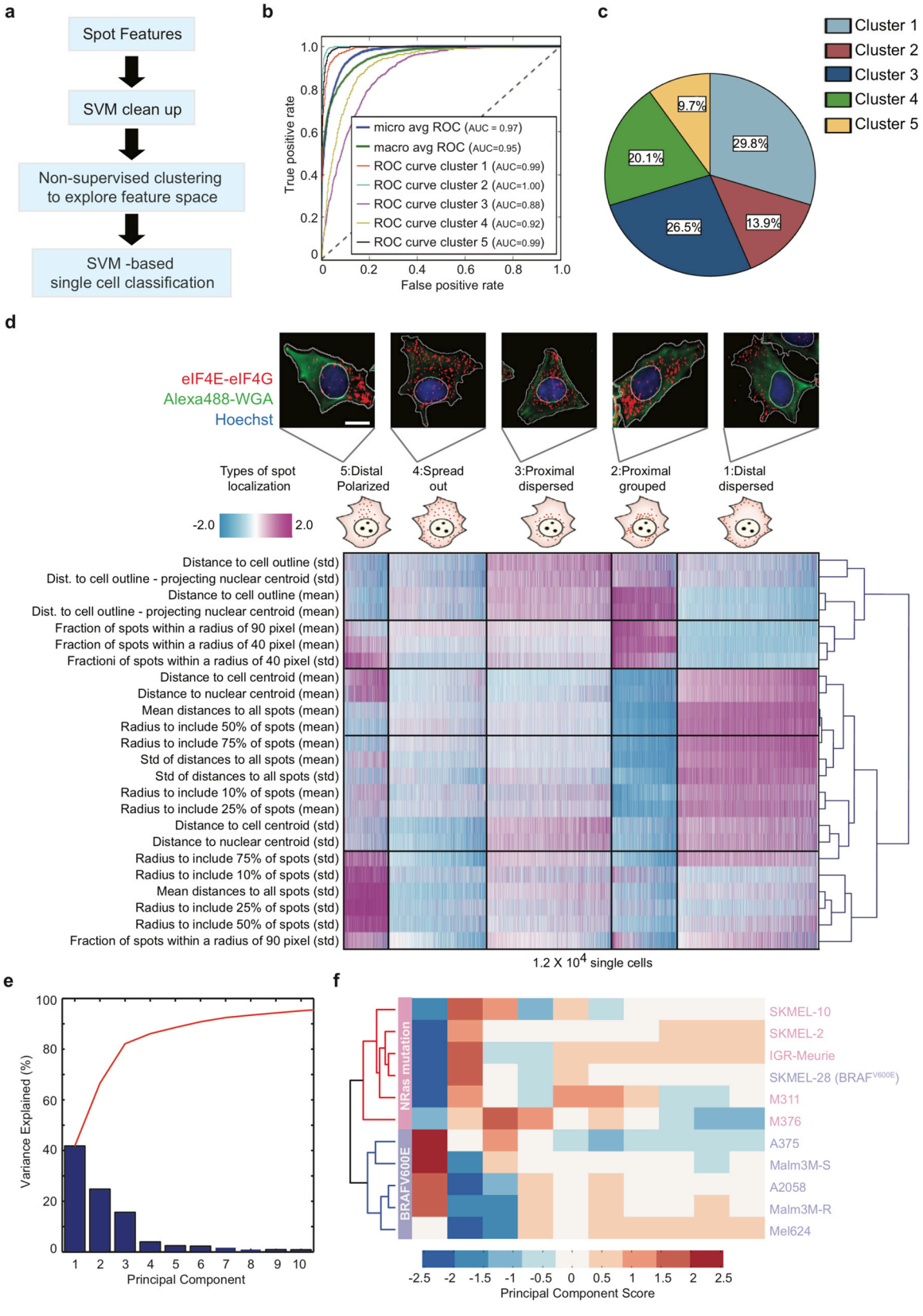

(caption on next page)

Fig. 3. Melanoma cell eIF4E-eIF4G spatial patterns determined by SVM-based machine learning. (A) The pipeline of the supervised machine learning. A SVM-based data clean-up process was used to eliminate in particular those cells in mitosis. We constructed a supervised SVM model by integrating the CellClassifier software developed in MATLAB. This cell-cycle related SVM data clean up resulted in a matrix of 1.2 × 104 cells. The matrix was then subjected to non-supervised clustering in order to determine the number clusters related to the different patterns of eIF4E-eIF4G complex intracellular localization. We integrated different packages of hierarchical classification methods (*i.e.* NbCluster, hclust, PvClust and WeightedCluster) from R into the SPSS modeler as a node of working flux, which allowed us to calculate the evolution of different indicators for the quality of the classification, and in turn determine the number of final clusters. Upon determination of the types of eIF4E-eIF4G complex localization patterns, we built a SVM-based classifier which is capable of classifying a single cell's eIF4E-eIF4G localization pattern into one of the five patterns. (B) The best classification model was multi-class SVM with a strategy one-*versus*-all. We classified the melanoma cells using this model, and calculated the Receiver operating curve test of the SVM model for each defined cluster. (C) The fraction of each phenocluster in all the analyzed melanoma cells. (D) Hierarchical clustering of the SVM-based spot features of 1.2×10^4 melanoma cells, and the corresponding localization pattern of the eIF4E-eIF4G complexes. Example images of cells corresponding to each type of eIF4E-eIF4G localization pattern are shown. (E) Dimension reduction of eIF4E-eIF4G complex spot features in order to cluster the melanoma cell lines based on their average spot features. Melanoma cell's eIF4E-eIF4G complex localization features were subjected to principal component analysis dimension reduction, and the top 10 principal components can explain 95.8% variance of the eIF4E-eIF4G complex localization patterns. These top 10 principal components were then further used as the input parameters for the cell line clustering as shown in (F). (F) Non-supervised hierarchical clustering of melanoma cell lines based on the top 10 principal components.

except one cell line (SKMEL-28). It included A375, Malme3M-S, A2058, Malme3M-R and Mel624. In addition, the two cell lines (A375 and Malme3M-S) sensitive to BRAF inhibition clustered closely together (Fig. 3**F**). In the other cluster, we found all the $NRAS^{Q61R}$ mutated melanoma cell lines except one BRAF mutated cell line, SKMEL-28 ($BRAF^{V600E}$/$CDK4^{R24C}$/$EGFR^{P753S}$/$PTEN^{T167A}$). SKMEL-28 is the only $BRAF^{V600E}$ mutated cell line harboring both EGFR and PTEN mutations, which could potentially bypass BRAF signaling to activate the downstream MAPK pathway. Although BRAF and NRAS mutations in melanoma are part of the same signaling axis, their mutations may lead to differential downstream signaling activation. NRAS mutated melanomas are to some extent sensitive to MEK inhibitors, but are more refractory to BRAF inhibition. In addition, NRAS oncogenic activation may also stimulate the PI3K/AKT pathway [31], which is known to be important for mRNA translational control [8]. Whether the differences in eIF4E-eIF4G localization patterns between BRAF and NRAS mutated melanoma cell lines represent differential translation of a subset of mRNAs needs further exploration. Nevertheless, our PLA-based image analysis shows that phenoclusters of eIF4E-eIF4G protein complexes can distinguish between melanoma cells harboring these different driver mutations.

2.6. Heterogeneity of eIF4E-eIF4G spatial patterns in melanoma cells

Our approach to define a landscape of eIF4E-eIF4G complex localization patterns at the single-cell level allowed us to probe the heterogeneity of eIF4F spatial patterns in each melanoma cell line. We thus took advantage of the SVM-based model and constructed a kernel density map of the five main phenoclusters (Fig. 4**A**), which could be used as an approximation of the melanoma mRNA translational "Waddington's landscape" [30]. Projecting all the single cells with different eIF4E-eIF4G spatial patterns onto the Kernel density map, we obtained the five phenoclusters as phenotype peaks (Fig. 4**B**). This allowed us to explore each melanoma cell line based on the kernel density of phenoclusters, showing that each melanoma cell line harbored a specific pattern of the eIF4E-eIF4G spatial landscape (Fig. 4**C**). Among all the melanoma cell lines tested, BRAF mutated cell lines known to be resistant to anti-BRAF targeted therapy, including A2058, Malme3M-R and Mel624, showed less heterogeneity in their eIF4E-eIF4G spatial patterns compared to cell lines sensitive to BRAF inhibition. Resistant cell lines also contained most of their cells in the eIF4E-eIF4G complexes spread out phenotype (Fig. 4**C**, left column). In particular, Mel624 was the most phenotypic homogeneous cell line, in which the majority of the cells showed the eIF4E-eIF4G spots spread out phenotype (cluster 4). In contrast, BRAF mutated cell lines (A375, SKMEL-28 and Malme3M-S) that were sensitive to anti-BRAF treatment showed a high variation of eIF4E-eIF4G complex spatial patterns. They contained cells showing a proximal dispersed phenotype (cluster 3), spread out phenotype (cluster 4), distal dispersed phenotype (cluster 1) and proximal grouped phenotype (cluster 2) (Fig. 4**C**, middle column). In the NRAS mutated melanoma cell lines, we observed an increased proximal grouped phenotype (cluster 2) in the M311, M376 and SKMEL-2 cell lines, whereas the IGR-Meurie and SKMEL-2 cell lines showed increased spread out and distal dispersed phenotypes (Fig. 4**C**, right column). These observations suggest that when a BRAF mutated cell shows a spread out eIF4E-eIF4G complex localization feature, it could be more refractory to BRAF inhibition. However, NRAS mutated cell lines showed a completely different variability of phenoclusters of the eIF4E-eIF4G complex, which might be due to differential signaling regulation related to the NRAS mutation. In addition, the BRAF/NRAS wild-type melanoma cell line MeWo showed a distinct pattern of eI4E-eIF4G localization, with a dominant distal polarized distribution (cluster 5) (Fig. 4**C**, lower right panel). To explore the specific mRNAs translated by the distinct spatial patterns of the eIF4F complexes, we interrogated the previously reported large-scale mRNA localization by smFISH [3]. Spread out localization of eIF4F mostly correlated with NADH-ubiquinone oxidoreductase family proteins, such as ND3, ND4, ND1 and ND5, and epithelial-mesenchymal transition associated factors, for instance TGFBR1, SERPINB5 and COX2 (Fig. 4**D**). Polarized distribution or distal dispersed localization of the eIF4F complex mainly correlated with mRNAs related to epigenetic factors, such as EZH2 and TRIO, and signaling proteins, such as RAPTOR and MDM2 (Fig. 4**E**). Translation of these mRNAs may be associated with melanoma cell chemoresistance since the COX2 and TGFB pathways are implicated in melanoma drug resistance [27,47].

To further explore the clinical relevance of the eIF4E-eIF4G localization features, we explored the eIF4E-eIF4G localization patterns in melanoma drug-tolerant persister cells [36]. Melanoma A375 cells were treated with DMSO or vemurafenib+cobimetinib (combo) for three days, then parental and persister cells were collected and subjected to drug-free culture for an additional nine days (Fig. 5**A**). We first confirmed that the melanoma persister cells were indeed resistant to combo re-challenge on day 1 (Fig. 5**B**). We then performed an eIF4E-eIF4G PLA assay on day 1, day 3 and day 9 during the drug-free culture. We found that melanoma persister cells showed a dominant spread out phenotype (cluster 4) of eIF4E-eIF4G localization, with minor localization patterns resembling cluster 5. However, upon drug-free culture after 9 days, melanoma persister-derived cells regained similar eIF4E-eIF4G localization features compared to those of the parental cells (Fig. 5**C**).

3. Discussion

In cells, specific localization of mRNAs provides the possibility for them to be translated hundreds of times in response to stimuli and is believed to be more energy-effective than transporting the individual protein products [10]. These specific subcellular localizations are generally coordinated with cellular status, which could potentially determine whether mRNAs are stored in a translationally suppressive state such as in stress granules or processing bodies (P-bodies). These localized mRNAs are primarily associated with RNA binding proteins, non-coding RNAs and translation regulatory factors [13]. Among the RNA-interacting factors, translation initiation factors, such as eIF4E, eIF4G and eIF4A, are often found within

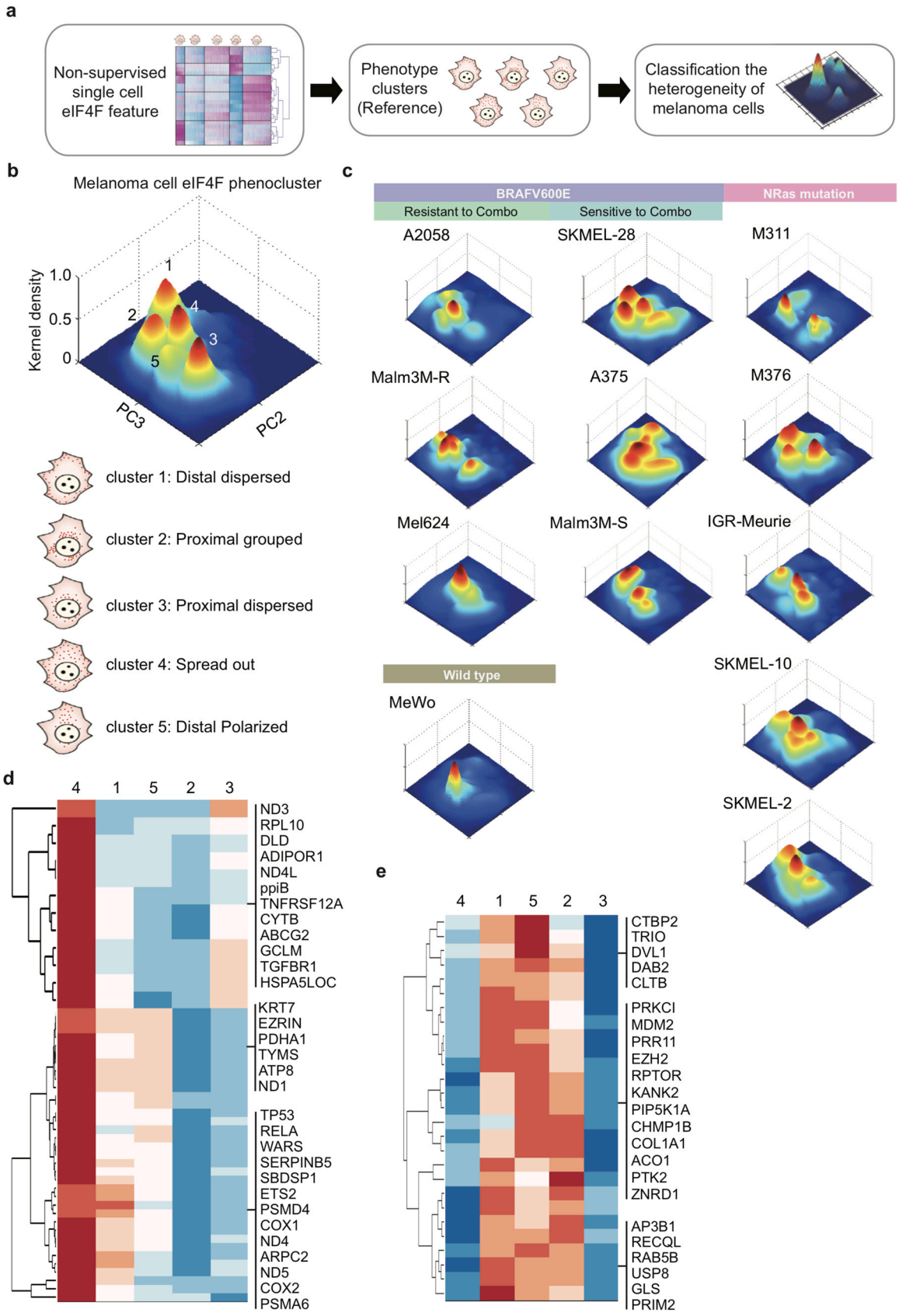

Fig. 4. Heterogeneity of eIF4E-eIF4G spatial patterns in melanoma cells. (A) The schematic view of the kernel density map projection. (B) The general kernel density map of all the melanoma cells and their corresponding phenoclusters. (C) The kernel density map of each melanoma cell line showing the heterogeneity of eIF4E-eIF4G complex spatial features. (D-E) Putative mRNAs translated at the corresponding spatial patterns of the eIF4E-eIF4G complexes based on a large-scale mRNA smFISH dataset [3].

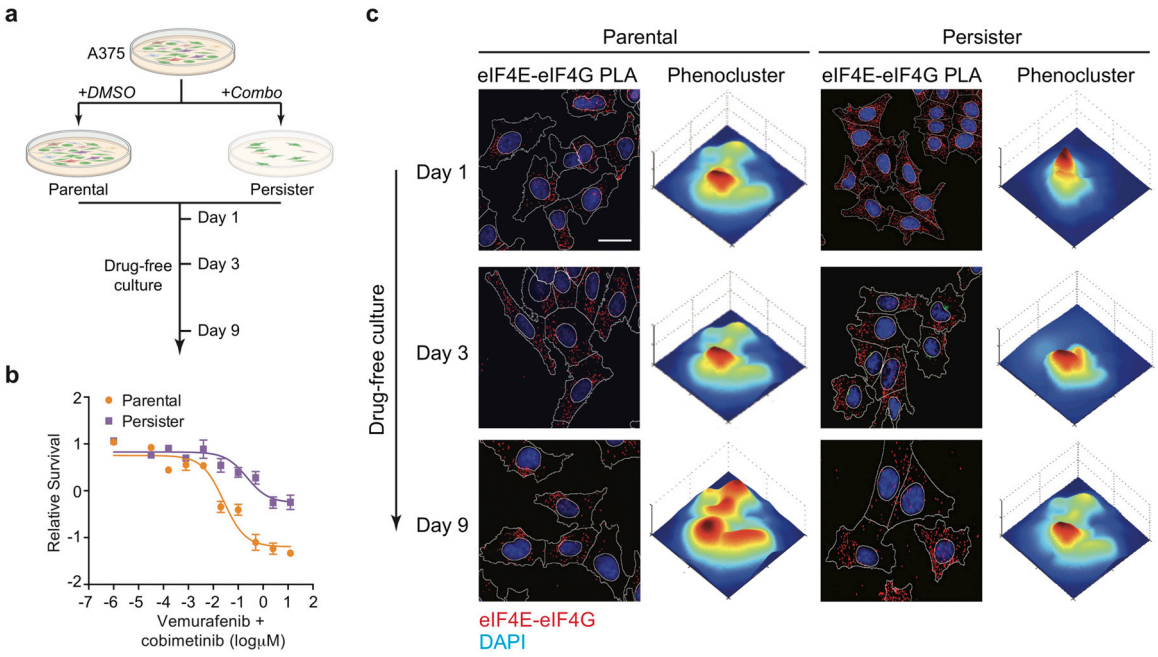

Fig. 5. Melanoma persister cells show distinct eIF4E-eIF4G localization patterns. (A) Schematic view of the generation of melanoma persister cells and the drug-free culture. (B) Cell viability assay to determine the resistance of melanoma persister cells to BRAF/MEK inhibition on day 1 in drug-free culture. (C) The eIF4E-eIF4G localization pattern in melanoma persister cells compared to that of the parental cells during 9-days of drug-free culture.

specific compartments together with mRNAs [16,6,7]. As a rate-limiting step of mRNA translation, the regulation of the eIF4F translation initiation complex offers cells a fast and flexible way to control protein expression and thus to adapt to environmental cues [11,12,44,8]. However, to our knowledge, no studies have systematically explored the spatial patterns of active *in situ* eIF4F translation initiation complexes in mammalian cells.

Most reports of the localization of eIF4F component proteins, such as eIF4E and eIF4G, have been based entirely on cell fractionation studies. Free eIF4G molecules are commonly well represented in cell extracts following gentle lysis, whereas extracts associated with eIF4E could be solubilized only in the presence of harsher anionic detergents. The methodological issues of studying localization of the eIF4F complex using cell fractionation is that lysis conditions may have unintended, selective effects on eIF4F complexes in mammalian cells. Mechanical lysis may even selectively deplete such complexes [4,40,41]. On the other side, microscopy studies have the advantage of conserving the localization of the protein complexes. Previous work studied the localization of eIF4E or eIF4G using immunofluorescence microscopy, which is very low resolution [45]. A recent study performed a dual protein-mRNA localization screen by using smFISH expressing GFP-tagged genes [9], which greatly increased the resolution of the localized mRNA translation. However, this study was not able to probe eIF4F complex localization in a systematic manner. In the current work, we took advantage of our previously developed PLA-based eIF4F *in situ* detection method [37] and adapted an image-based analysis pipeline to study eIF4F complex spatial patterning in human melanoma cells. By using a supervised machine learning algorithm, we defined five macro phenoclusters of the eIF4F complex in eleven melanoma cells harboring different driver mutations.

We found that, at least in human melanoma cells, active eIF4F translation initiation complexes showed extremely high inter- and intra-cellular levels of heterogeneity in terms of spatial intracellular distribution. We observed grouped or dispersed perinuclear localization of eIF4F accounting for 40.4% of all the cells (Fig. 3**C**), and dispersed or polarized distal localization representing 39.5% of total cells. And the rest showed a more spread-out cytoplasmic distribution (20.1%). By using kernel density approximation, we showed that, even in the genetically identical cells, eIF4F complexes distribute to different subcellular localizations in individual cells (Fig. 4**C**). This is different from what has been observed in developmental embryos, in which the mRNA translation spatial patterns appear much more stereotyped [18]. This could be due to the oncogenic mutation-driven signaling pathway dysfunctions that may change the activity or variation of local mRNA translation. Indeed, we found that the spatial pattern of eIF4F complexes could potentially distinguish $BRAF^{V600E}$ and $NRAS^{Q61R}$ mutated melanoma cells (Fig. 3**F**). Although NRAS and BRAF mutations both activate the downstream MAPK pathway, which may directly impact the activity of eIF4F regulators such as MNK1/2 [14], NRAS can also regulate the PI3K/AKT pathway, which bypasses the RAS-BRAF-MEK signaling axis. The pleotropic downstream signaling relayed by NRAS mutations may activate both phosphorylation of ERK and mTOR-S6K1/2 [15], thus leading to differential regulation of mRNA translation activity. eIF4F activity was also shown to be involved in the drug resistance of melanoma cells [5,36]. Our results show that different melanoma cell lines showed heterogeneous subpopulations of cells with distinct spatial patterns of eIF4F, and the localized translation of a subset of mRNAs that may be related to the variation in sensitivity to targeted therapy in melanoma [36,43]. This hypothesis needs to be further explored in the future by taking into account the spatial variations of mRNA translation.

The limitation of our current study is that the observations are based on *in vitro* models. *In vivo,* the spatio-temporal regulation of eIF4F would not only be regulated by cell-intrinsic signaling activities, but cell-cell contacts and extracellular factors may also impact the activity and localization of eIF4F translation initiation complexes. In addition, our method requires precise quantification of each single dot in a well identified cell, which is quite challenging *in vivo*. It would be favorable to combine our approach with proteomic methods that determine absolute protein abundances, for example the minimal, encapsulated proteomic-sample processing method developed by Kulak and colleagues [24]. On the other hand, it is known that cells at the G2/M phase or in mitosis translate at around 25% the rate of interphase cells, which is partially due to inhibition

of the translation initiation step following the hypophosphorylation of eIF4E [33]. Although we have eliminated those cells at mitosis by using a supervised machine learning method [34], our current pipeline could not exclude the impact on eIF4E-eIF4G localization patterns from cells existing at different time points of interphase. Future studies should further integrate co-staining of cell-cycle markers with the eIF4E-eIF4G PLA assay or implement cell cycle inference computational methods on fixed cells [19]. Notwithstanding these limitations, our work opens new perspectives to study the spatial regulation of the mRNA translation machinery in pathophysiological contexts by studying patients' biopsies using similar *ex vivo* labeling associated with imaging technologies. Adapting this technology to patient's tumor samples could potentially open new avenues and provide new information on tumor cell status beyond somatic genetic events. Monitoring eIF4F phenoclusters could thus become a helpful predictive or monitoring tool for cancer treatment.

4. Materials and methods

Cell cultures and reagents. The melanoma cell lines used in this study, including BRAFV600E mutated cell lines such as A2058, A375, Malm3M, Mel624 and SKMEL-28, and NRAS mutated cell lines such as SKMEL-10, SKMEL-2, M376 and M311, were purchased from the ATCC. IG-Meurie cell line is kindly provided by Prof Caroline Robert (Gustave Roussy, France). All the cell lines were maintained at 37 °C and 5% CO_2 in a humidified atmosphere and grown in DMEM growth media supplemented with 10% FBS, 2 mM glutamine (Gibco), except for SK-Mel-28 cells were grown in RPMI supplemented with 10% FBS. All cell lines were regularly controlled to be mycoplasma-free by using a PCR-based test (Minerva Biolabs). BRAF inhibitor (Vemurafenib, #S1267), mTOR inhibitor (PP242, #S2218) were purchased from selleckchem (Euromedex, France). For nutrient starvation, cells were cultured in HBSS (#55037 C, Merck, China) for 2 h.

Polysome profiling for translation activity measurement. Polysome profiling was performed as described previously [5,17]. Briefly, cells with indicated treatment were incubated at 37 °C with 100 μg/mL cycloheximide in fresh medium for 5 min. Cells were then washed, scraped into ice-cold PBS supplemented with 100 μg/mL cycloheximide, centrifuged at 3000 r.p.m. for 5 min. The cell pellets were resuspended into 400 μL of LSB buffer (5 mM Tris, pH 7.5, 1.5 mM KCl, 2.5 mM $MgCl_2$, 2 mM DTT, 100 U/mL RNasin, 1x protease and phosphatase cocktail inhibitors and 100 μg/mL cycloheximide). After homogenization, 400 μL LSB buffer supplemented with 0.5% Triton X-100% and 0.5% sodium deoxycholate was added to a total volume of 500 μL. Samples were stayed on ice for 30 min and centrifuged at 12,000 g for 15 min at 4 °C. The lysates were then measured by nanoDrop and normalized by adding hypotonic buffer based on the OD_{260} value. Sucrose gradient was prepared as follows: Prepare 100 mL of 60% (w/v) sucrose solution in ddH_2O. Solution should be filtered through a 0.22 μm filter to prevent clogging of the tubing. Prepare 5 mL of 10x sucrose gradient buffer: 200 mM HEPES (pH 7.6), 1 M KCl, 50 mM $MgCl_2$, 100 μg/mL cycloheximide, 1x protease inhibitor cocktail (EDTA-free), 100 U/mL RNase inhibitor. Using the 60% solution prepared as described above, make 40 mL of 5% and 50% sucrose solutions in 1x sucrose gradient buffer and make the density gradient on the Gradient master machine. The normalized lysates were then loaded onto a 5–50% sucrose density gradient and centrifuged in an SW41 Ti rotor (Beckman) at 36,000 r.p.m. for 2 h at 4 °C. Polysome fractions were monitored and collected using a gradient fractionation system (Isco).

Proximity ligation assay. Interactions between eIF4E and eIF4G (eIF4E-eIF4G) were detected by *in situ* proximity ligation assay (PLA) [5]. Cells were fixed in 4% paraformaldehyde at room temperature for 12 min and were permeabilized with 0.5% Triton X-100 in PBS at room temperature for 15 min. The PLA protocol was followed according to the manufacturer's procedure (Olink Bioscience). Briefly, fixed cells were incubated with blocking buffer (Olink Bioscience) at 37 °C for 20 min, and then were hybridized with primary antibodies eIF4E (mouse, clone A-10, SC-271480, Santa Cruz Biotechnology, 1:200) and eIF4G (rabbit, #2498; Cell Signaling Technology, 1:200) in antibody diluent (Olink Bioscience) at 37 °C for 1 h. Cells were then washed twice with Buffer A (Olink Bioscience), and were incubated with secondary probes (Olink Bioscience) at 37 °C for 1 h. After 30 min incubation with T4 ligase, *in situ* circular PCR amplification was performed at 37 °C for 1 h. Cells were then stained with Alexa488-phalloidin (#A12379, ThermoFisher Scientific, 1:1000) for 15 min at room temperature. Cells were mounted with anti-fade mounting oil supplemented with DAPI. Images were acquired on Olympus Scanner System (VS120) with 20 X objective (1 pixel = 0.32 μm). Images were then analyzed in CellProfiler 2.0.

RNA interference. Cells were transfected with 20 nM of each siRNA using Lipofectamine RNAiMAX Reagent (Life Technologies) following the supplier's instructions. siRNAs were purchased from Thermo Scientific (ON-TARGETplus technology). The RNAi were used from the same siRNAs as previously reported [37].

EIF4E-eIF4G proximity ligation assay single cell image analyses. All the images were analyzed with the image analysis software CellProfiler[29], based on MATLAB_R2011a version (7.12.0.635 version, 64-bit). Nuclei were segmented using images from Hoechst 33342 staining. The cell outlines were then identified using the propagation and watershed algorithm in Cellprofiler modules. EIF4E-eIF4G PLA spot detection was performed by following steps: all the images were firstly corrected by Cellprofiler module 'illumination correction' and thus rescaled intensities were calculated automatically based on all the analyzed images. For spot detection, we performed a Laplacian-of-Gaussian (LoG) filter to the rescaled images and defined all objects above a certain threshold as spots. We used one global threshold for all images after ensuring that corrected intensities of individual images were comparable. The specific threshold value was chosen from 40 random images. To avoid dim images and false-positive spots, at least one pixel within a spot was required to have an intensity which would be above the permitted range of the minimal intensity of an image. To further segment the highly crowded spots, intensity-based deblending was done to separate local peaks in each image. This was adapted by a deblending function originated from the astrophysics software SourceExtractor [3], with a minor modification in which a linear scale for deblending was used.

Analyses of cellular patterns of eIF4E-eIF4G PLA spot localization. Primary spot features were calculated by the 'MasureLocalizationOfSpots.m' Cellprofiler module. This comprises 18 primary features in total, in which only 16 were used for the following analysis: including 1) closest distance to membrane; 2) distance to cell centroid; 3) distance to nuclear centroid; 4) distance to cell outline projecting from nuclear centroid; 5) each spot mean distance to remaining spots; 6) standard deviation of each spot distance to remaining spots; 7) radius in pixels to include 5%, 10%, 25%, 50% or 75% of all remaining spots in each cell; 8) number of spots within 20, 40, 80 and 120 pixels from a given spot center; 9) the mean and standard deviation of 7) and 8) features were calculated and normalized to the square root of the area of a given cell; Meanwhile, we also measured the cell features, including cell area shape, cell major and minor axis, nuclear area shape and nuclear axis, and Zernik cell features (Fig. 1).

EIF4E-eIF4G PLA spot feature preparation for multivariate analysis. Primary eIF4E-eIF4G PLA spot features were obtained by the 'MeasureLocalizationOfSpots.m' Cellprofiler module. Measurements of individual eIF4E-eIF4G PLA spots were normalized by z-scoring against random cytoplasmic pixels. The number of sampled pixels were the same as the number of spots, which were originally identified in the given cell. Sampling of pixels was iterated

100 times. Per iteration, the measurements of a single random pixel were used for the normalization of measurements of a given observed eIF4E-eIF4G PLA spot. To general each cell's eIF4E-eIF4G PLA spot features, cellular features were obtained by the 'MeasureChildren.m′ Cellprofiler module. For each parent objects (Cells), measurements robust to NaN (not a number) were derived from the normalized primary features of its corresponding children (eIF4E-eIF4G PLA spots). The corresponding statistics measured were mean, median, standard deviation and variance as well was third, fourth, fifth and sixth central moments. However, for each cell, only eIF4E-eIF4G PLA spot measurements that were not NaN, was considered for the calculation of the central moments.

Non-supervised single cell clustering. 1.5×10^4 cells were randomly sampled from the initial pool of cells and the pairwise Euclidean distance to a randomly sampled 20% of the $\sim1.5\times10^4$ cells was computed in the full eIF4E-eIF4G PLA spot feature space after z-score normalization. The number of neighbors of every cell was calculated. We iterated this sampling process to achieve ~ 2000 cell samplings and non-supervised hierarchical clustering was done using a Euclidean distance and Ward's linkage method. The non-supervised clustering was implemented in SPSS software in order to determine the number groups, and followed K-means for the partition of the dataset.

Supervised classification of eIF4E-eIF4G localization patterns. Ensemble non-supervised clustering identified five eIF4E-eIF4G PLA spot localization patterns. Classification was based on this non-supervised clustering as references. The z-score normalized image analysis data were randomly divided into two part, including 70% of individual cells as training dataset and 30% of the remaining individual cells as validation dataset. We thus manually built a training dataset derived from A375 cell line from each of the five localization patterns, corresponding to the five clusters respectively. We trained the dataset by different machine learning methods, including K-means neighbor classifier, support vector machine (SVM, linear nuclear and Gaussian nuclear), random forest and gradient boosting classifier. Each method was evaluated by validation dataset to obtain their confusion matrix, ROC curve for the TVP and TFP calculation. All the processes were performed in R. By comparing all the methods, we determined the best classifier, multi-class SVM with one *versus* all strategy.

Code availability. In this study we did not develop novel computational code for the analyses. The spot quantification pipeline could be found on the website: https://sites.google.com/site/translationcomplexeif4f/home [37]. For the MATLAB-based Cellprofiler pipeline, we used the Cellprofiler modules in combination with the modules developed by Lucas Pelkmans's lab [3]. We shared the 'MeasureLocalizationOfSpots.m′ file in the supplemental files, however, please refer to the work from Battich et al. Battich et al., [3] when using this code.

Author statement

Y.P., X.T., S.S. and C.R. designed research; Y.P., X.T., S.F. H.P., T.L., K.L., D.P. performed research; Y.P., X.T., M.C., D.P., S.S., L.L. performed the analyses; J.X., L.L., C.R. and S.S. wrote the paper.

Conflict of interest statement

C.R. is founder of RiboNexus Therapeutics (France). C.R. receives consulting income from BMS, MSD, Roche, Novartis, AstraZeneca, Sanofi and Pierre Fabre. No disclosures were reported by other authors.

Acknowledgements

We thank Ensemble contre le Mélanome; The Foundation Crédit Mutuel, The Foundation Carrefour, Olivier and Christian Courtin and the association Vaincre le Mélanome for their constant support (C.R.). S.S. is supported by the Natural Science Foundation of China (NSFC, 82172794) and National Clinical Research Center for Geriatrics, West China Hospital, Sichuan University (grant no. Y2022JC002). S.S. thanks the constant support from Sébastien Bazin. We acknowledge the editing support of Life Science Editors.

Appendix A. Supporting information

Supplementary data associated with this article can be found in the online version at doi:10.1016/j.csbj.2023.01.040.

References

[1] Aviram N, Schuldiner M. Targeting and translocation of proteins to the endoplasmic reticulum at a glance. J Cell Sci 2017;130:4079–85.
[2] Barbarese E, Koppel DE, Deutscher MP, Smith CL, Ainger K, Morgan F, Carson JH. Protein translation components are colocalized in granules in oligodendrocytes. J Cell Sci 1995;108(Pt 8):2781–90.
[3] Battich N, Stoeger T, Pelkmans L. Image-based transcriptomics in thousands of single human cells at single-molecule resolution. Nat Methods 2013;10:1127–33.
[4] Bergamini G, Preiss T, Hentze MW. Picornavirus IRESes and the poly(A) tail jointly promote cap-independent translation in a mammalian cell-free system. RNA 2000;6:1781–90.
[5] Boussemart L, Malka-Mahieu H, Girault I, Allard D, Hemmingsson O, Tomasic G, Thomas M, Basmadjian C, Ribeiro N, Thuaud F, et al. eIF4F is a nexus of resistance to anti-BRAF and anti-MEK cancer therapies. Nature 2014;513:105–9.
[6] Brengues M, Parker R. Accumulation of polyadenylated mRNA, Pab1p, eIF4E, and eIF4G with P-bodies in Saccharomyces cerevisiae. Mol Biol Cell 2007;18:2592–602.
[7] Buchan JR, Yoon JH, Parker R. Stress-specific composition, assembly and kinetics of stress granules in Saccharomyces cerevisiae. J Cell Sci 2011;124:228–39.
[8] Cerezo M, Robert C, Liu L, Shen S. The role of mRNA translational control in tumor immune escape and immunotherapy resistance. Cancer Res 2021;81:5596–604.
[9] Chouaib R, Safieddine A, Pichon X, Imbert A, Kwon OS, Samacoits A, Traboulsi AM, Robert MC, Tsanov N, Coleno E, et al. A dual protein-mRNA localization screen reveals compartmentalized translation and widespread co-translational RNA targeting. Dev Cell 2020;54(773–791):e775.
[10] Das S, Vera M, Gandin V, Singer RH, Tutucci E. Intracellular mRNA transport and localized translation. Nat Rev Mol Cell Biol 2021;22:483–504.
[11] Donlin-Asp PG, Polisseni C, Klimek R, Heckel A, Schuman EM. Differential regulation of local mRNA dynamics and translation following long-term potentiation and depression. Proc Natl Acad Sci USA 2021:*118*.
[12] Donnelly CJ, Willis DE, Xu M, Tep C, Jiang C, Yoo S, Schanen NC, Kirn-Safran CB, van Minnen J, English A, et al. Limited availability of ZBP1 restricts axonal mRNA localization and nerve regeneration capacity. EMBO J 2011;30:4665–77.
[13] Engel KL, Arora A, Goering R, Lo HG, Taliaferro JM. Mechanisms and consequences of subcellular RNA localization across diverse cell types. Traffic 2020;21:404–18.
[14] Fabbri L, Chakraborty A, Robert C, Vagner S. The plasticity of mRNA translation during cancer progression and therapy resistance. Nat Rev Cancer 2021;21:558–77.
[15] Fedorenko IV, Gibney GT, Smalley KS. NRAS mutant melanoma: biological behavior and future strategies for therapeutic management. Oncogene 2013;32:3009–18.
[16] Ferraiuolo MA, Basak S, Dostie J, Murray EL, Schoenberg DR, Sonenberg N. A role for the eIF4E-binding protein 4E-T in P-body formation and mRNA decay. J Cell Biol 2005;170:913–24.
[17] Gandin V, Sikstrom K, Alain T, Morita M, McLaughlan S, Larsson O, Topisirovic I. Polysome fractionation and analysis of mammalian translatomes on a genome-wide scale. J Vis Exp 2014.
[18] Groisman I, Huang YS, Mendez R, Cao Q, Theurkauf W, Richter JD. CPEB, maskin, and cyclin B1 mRNA at the mitotic apparatus: implications for local translational control of cell division. Cell 2000;103:435–47.
[19] Gut G, Tadmor MD, Pe'er D, Pelkmans L, Liberali P. Trajectories of cell-cycle progression from fixed cell populations. Nat Methods 2015;12:951–4.
[20] Janes MR, Limon JJ, So L, Chen J, Lim RJ, Chavez MA, Vu C, Lilly MB, Mallya S, Ong ST, et al. Effective and selective targeting of leukemia cells using a TORC1/2 kinase inhibitor. Nat Med 2010;16:205–13.
[21] Jung H, Gkogkas CG, Sonenberg N, Holt CE. Remote control of gene function by local translation. Cell 2014;157:26–40.
[22] Kedersha NL, Gupta M, Li W, Miller I, Anderson P. RNA-binding proteins TIA-1 and TIAR link the phosphorylation of eIF-2 alpha to the assembly of mammalian stress granules. J Cell Biol 1999;147:1431–42.
[23] Knowles RB, Sabry JH, Martone ME, Deerinck TJ, Ellisman MH, Bassell GJ, Kosik KS. Translocation of RNA granules in living neurons. J Neurosci 1996;16:7812–20.
[24] Kulak NA, Pichler G, Paron I, Nagaraj N, Mann M. Minimal, encapsulated proteomic-sample processing applied to copy-number estimation in eukaryotic cells. Nat Methods 2014;11:319–24.
[25] Lawrence JB, Singer RH. Intracellular localization of messenger RNAs for cytoskeletal proteins. Cell 1986;45:407–15.

[26] Lindemann S, Tolley ND, Eyre JR, Kraiss LW, Mahoney TM, Weyrich AS. Integrins regulate the intracellular distribution of eukaryotic initiation factor 4E in platelets. A checkpoint for translational control. J Biol Chem 2001;276:33947–51.
[27] Liu S, Ren J, Ten Dijke P. Targeting TGFbeta signal transduction for cancer therapy. Signal Transduct Target Ther 2021;6:8.
[28] Malka-Mahieu H, Newman M, Desaubry L, Robert C, Vagner S. Molecular pathways: the eIF4F translation initiation complex-new opportunities for cancer treatment. Clin Cancer Res 2017;23:21–5.
[29] McQuin C, Goodman A, Chernyshev V, Kamentsky L, Cimini BA, Karhohs KW, Doan M, Ding L, Rafelski SM, Thirstrup D, et al. CellProfiler 3.0: next-generation image processing for biology. PLoS Biol 2018;16:e2005970.
[30] Moris N, Pina C, Arias AM. Transition states and cell fate decisions in epigenetic landscapes. Nat Rev Genet 2016;17:693–703.
[31] Oikonomou E, Koustas E, Goulielmaki M, Pintzas A. BRAF vs RAS oncogenes: are mutations of the same pathway equal? Differential signalling and therapeutic implications. Oncotarget 2014;5:11752–77.
[32] Pool MR. Targeting of proteins for translocation at the endoplasmic reticulum. Int J Mol Sci 2022:*23*.
[33] Pyronnet S, Dostie J, Sonenberg N. Suppression of cap-dependent translation in mitosis. Genes Dev 2001;15:2083–93.
[34] Ramo P, Sacher R, Snijder B, Begemann B, Pelkmans L. CellClassifier: supervised learning of cellular phenotypes. Bioinformatics 2009;25:3028–30.
[35] Regot S, Hughey JJ, Bajar BT, Carrasco S, Covert MW. High-sensitivity measurements of multiple kinase activities in live single cells. Cell 2014;157:1724–34.
[36] Shen S, Faouzi S, Bastide A, Martineau S, Malka-Mahieu H, Fu Y, Sun X, Mateus C, Routier E, Roy S, et al. An epitranscriptomic mechanism underlies selective mRNA translation remodelling in melanoma persister cells. Nat Commun 2019;10:5713.
[37] Shen S, Girault I, Malka-Mahieu H, Robert C, Vagner S. In situ detection of the eIF4F translation initiation complex in mammalian cells and tissues. STAR Protoc 2021;2:100621.
[38] Shen S, Niso-Santano M, Adjemian S, Takehara T, Malik SA, Minoux H, Souquere S, Marino G, Lachkar S, Senovilla L, et al. Cytoplasmic STAT3 represses autophagy by inhibiting PKR activity. Mol Cell 2012;48:667–80.
[39] Smart FM, Edelman GM, Vanderklish PW. BDNF induces translocation of initiation factor 4E to mRNA granules: evidence for a role of synaptic microfilaments and integrins. Proc Natl Acad Sci USA 2003;100:14403–8.
[40] Svitkin YV, Imataka H, Khaleghpour K, Kahvejian A, Liebig HD, Sonenberg N. Poly (A)-binding protein interaction with eIF4G stimulates picornavirus IRES-dependent translation. RNA 2001;7:1743–52.
[41] Svitkin YV, Sonenberg N. An efficient system for cap- and poly(A)-dependent translation in vitro. Methods Mol Biol 2004;257:155–70.
[42] Van Driesche SJ, Martin KC. New frontiers in RNA transport and local translation in neurons. Dev Neurobiol 2018;78:331–9.
[43] Vendramin R, Katopodi V, Cinque S, Konnova A, Knezevic Z, Adnane S, Verheyden Y, Karras P, Demesmaeker E, Bosisio FM, et al. Activation of the integrated stress response confers vulnerability to mitoribosome-targeting antibiotics in melanoma. J Exp Med 2021:*218*.
[44] Verma P, Chierzi S, Codd AM, Campbell DS, Meyer RL, Holt CE, Fawcett JW. Axonal protein synthesis and degradation are necessary for efficient growth cone regeneration. J Neurosci 2005;25:331–42.
[45] Willett M, Flint SA, Morley SJ, Pain VM. Compartmentalisation and localisation of the translation initiation factor (eIF) 4F complex in normally growing fibroblasts. Exp Cell Res 2006;312:2942–53.
[46] Woods AJ, Roberts MS, Choudhary J, Barry ST, Mazaki Y, Sabe H, Morley SJ, Critchley DR, Norman JC. Paxillin associates with poly(A)-binding protein 1 at the dense endoplasmic reticulum and the leading edge of migrating cells. J Biol Chem 2002;277:6428–37.
[47] Zelenay S, van der Veen AG, Bottcher JP, Snelgrove KJ, Rogers N, Acton SE, Chakravarty P, Girotti MR, Marais R, Quezada SA, et al. Cyclooxygenase-dependent tumor growth through evasion of immunity. Cell 2015;162:1257–70.